The Astronomical Journal, 168:13 (13pp), 2024 July https://doi.org/10.3847/1538-3881/ad4964
© 2024. The Author(s). Published by the American Astronomical Society.
OPEN ACCESS

HIP 65426 is a High-frequency Delta Scuti Pulsator in Plausible Spin–Orbit Alignment with its Directly Imaged Exoplanet

Aldo G. Sepulveda[1,5], Daniel Huber[1,2], Timothy R. Bedding[2], Daniel R. Hey[1], Simon J. Murphy[3], Zhoujian Zhang[4,6], and Michael C. Liu[1]
[1] Institute for Astronomy, University of Hawai'i at Mānoa. 2680 Woodlawn Drive, Honolulu, HI 96822, USA; aldo.sepulveda@hawaii.edu
[2] Sydney Institute for Astronomy (SIfA), School of Physics, University of Sydney, NSW 2006, Australia
[3] Centre for Astrophysics, University of Southern Queensland, Toowoomba, QLD 4350, Australia
[4] Department of Astronomy and Astrophysics, University of California, Santa Cruz, CA 95064, USA
Received 2023 November 23; revised 2024 May 3; accepted 2024 May 7; published 2024 June 18

Abstract

HIP 65426 hosts a young giant planet that has become the first exoplanet directly imaged with JWST. Using time-series photometry from the Transiting Exoplanet Survey Satellite (TESS), we classify HIP 65426 as a high-frequency δ Scuti pulsator with a possible large-frequency separation of $\Delta\nu = 7.23 \pm 0.02$ cycles day^{-1}. We check the TESS data for pulsation-timing variations and use the nondetection to estimate a 95% dynamical mass upper limit of 12.8 $M_{\rm Jup}$ for HIP 65426 b. We also identify a low-frequency region of signal that we interpret as stellar latitudinal differential rotation with two rapid periods of 7.85 ± 0.08 hr and 6.67 ± 0.04 hr. We use our TESS rotation periods together with published values of radius and $v \sin i$ to jointly measure the inclination of HIP 65426 to $i_\star = 107^{+12}_{-11}{}^\circ$. Our stellar inclination is consistent with the orbital inclination of HIP 65426 b ($108^{+6}_{-3}{}^\circ$) at the 68% percent level based on our orbit fit using published relative astrometry. The lack of significant evidence for spin–orbit misalignment in the HIP 65426 system supports an emerging trend consistent with preferential alignment between imaged long-period giant planets and their host stars.

Unified Astronomy Thesaurus concepts: Delta Scuti variable stars (370); Exoplanet systems (484); Planet hosting stars (1242); Stellar pulsations (1625)

1. Introduction

HIP 65426 (HD 116434, TIC 438702139) is a nearby (107.5 ± 0.4 pc, Gaia Collaboration et al. 2016, 2021) A2 V star (Houk 1978) that hosts a directly imaged giant planet (HIP 65426 b; Chauvin et al. 2017). The host star is a member of the Lower Centaurus-Crux (LCC) young moving group (de Zeeuw et al. 1999; Luhman 2022), with an age of ~10–23 Myr (e.g., Mamajek et al. 2002; Sartori et al. 2003; Pecaut et al. 2012; Song et al. 2012). Independent of its membership in LCC, Chauvin et al. (2017) derived an age of 14 ± 4 Myr for HIP 65426 primarily using isochrone fitting. HIP 65426 has several astrophysically interesting qualities in addition to being an exoplanet host star. Its $v \sin i$ (261–299 km s^{-1}, Chauvin et al. 2017; Petrus et al. 2021) indicates that it is rapidly rotating. Hints of stellar pulsations have been identified in its radial velocity variations (e.g., Chauvin et al. 2017; Grandjean et al. 2020; Petrus et al. 2021), but HIP 65426's variability status has not yet been formally confirmed and classified. A detection of high-frequency δ Scuti pulsations would independently confirm HIP 65426's youth (Bedding et al. 2020) and might even enable an asteroseismic age to be measured (e.g., Murphy et al. 2021; Steindl et al. 2022).

The giant planet HIP 65426 b orbits at a semimajor axis of 62–120 au and inclined 99°–112° to the line of sight based on orbit-fitting analyses (Cheetham et al. 2019; Bowler et al. 2020; Blunt et al. 2023; Carter et al. 2023; Do et al. 2023). Mass estimates of HIP 65426 b, derived from evolution models and from spectral fitting, span 6–11 $M_{\rm Jup}$(Chauvin et al. 2017; Cheetham et al. 2019; Marleau et al. 2019; Petrus et al. 2021; Carter et al. 2023). HIP 65426 was recently observed with NIRCam and MIRI as part of the JWST (Gardner et al. 2006, 2023) Early Release Science Program (Hinkley et al. 2022), resulting in HIP 65426 b becoming the first direct detection of an exoplanet at wavelengths beyond 5 μm (Carter et al. 2023).

Assessment of the spin–orbit alignment between a host star and its orbiting companions (i.e., obliquity) provides insight into the dynamical history of the system. While obliquity measurements have been obtained for dozens of short-period transiting exoplanets (e.g., Albrecht et al. 2022), there are relatively few constraints for long-period imaged substellar companions (e.g., Bowler et al. 2017; Bryan et al. 2020; Kraus et al. 2020). Recently, Bowler et al. (2023) analyzed the spin–orbit alignments for a sample of 23 imaged substellar companions orbiting cool stars by constraining the stellar inclinations and comparing to the companion orbital inclinations. They found that misalignments are common for their sample, which mostly comprised brown dwarfs. However, the two imaged giant planet systems in their sample were consistent with alignment or near-alignment. Determining whether or not additional imaged giant planets like HIP 65426 b are aligned with their host star would contribute to our understanding of giant planet formation as a population, as well as help to clarify the dynamical history for the planet itself.

Time-series photometry from the Transiting Exoplanet Survey Satellite (TESS; Ricker et al. 2015) is continuing to boost the sample size of systems where obliquity assessments

[5] NSF Graduate Research Fellow.
[6] NASA Sagan Fellow.

Original content from this work may be used under the terms of the Creative Commons Attribution 4.0 licence. Any further distribution of this work must maintain attribution to the author(s) and the title of the work, journal citation and DOI.

can be carried out. Time-series photometry can reveal the stellar rotation period if surface spot modulation is significant (e.g., Affer et al. 2012; McQuillan et al. 2014). While this has traditionally been carried out for cool stars, Balona (2011, 2013, 2017) used Kepler time-series photometry to show that as many as ∼40% of A-type stars exhibit a detectable photometric rotation frequency. This fraction persists to ∼30% when source contamination is considered (Sikora et al. 2020). A measured rotation period places a determination on the line-of-sight inclination when combined with the stellar radius and spectroscopic projected rotational velocity ($v \sin i$), (e.g., Masuda & Winn 2020). Furthermore, time-series photometry also probes for other phenomena, including stellar pulsations and transit events, both of which have previously been studied in directly imaged exoplanet host stars using TESS (e.g., Zieba et al. 2019; Pavlenko et al. 2022; Sepulveda et al. 2022, 2023). The challenge for hot A stars like HIP 65426 then becomes a matter of detecting a rotation frequency and discerning it from other phenomena, such as pulsation modes or contaminating sources in the aperture.

We analyze 2 minutes cadence TESS time-series photometry of HIP 65426 in this study. We present the detection of stellar pulsations and rotational modulation in the data, and use the latter to constrain the obliquity of the system. We conclude by summarizing the implications of our analysis.

2. TESS Observations

HIP 65426 was observed by TESS in 2 minutes cadence mode for Sectors 11, 38, and 64. The gaps between these sectors are ∼2 yr. Sector 11 observations spanned UTC 2019 April 23–2019 May 20, Sector 38 spanned UTC 29 April 2021–26 May 2021, and Sector 64 spanned UTC 2023 April 6–2023 May 4. We used `lightkurve` (Lightkurve Collaboration et al. 2018) to download PDC-SAP light curves processed by SPOC (Smith et al. 2012; Stumpe et al. 2012, 2014; Jenkins et al. 2016). We removed outlying photometry from each TESS sector via a sigma-clipping of five standard deviations from the median flux value, which is a standard practice to remove outliers potentially caused by instrumental artifacts that were not captured through standard quality flags. This resulted in only 21 cadences (<0.05%) being removed, resulting in 16,392 cadences for Sector 11, 18,486 cadences for Sector 38, and 18,849 cadences for Sector 64.

We assessed our TESS data for any significant sources of contamination. We began by inspecting a region within a radius of 80″ from HIP 65426, which is an approximate size of the default aperture used for our light curves. We identified no Gaia sources with comparable brightness to HIP 65426, which has an apparent Gaia G-band magnitude of 7.00 (Gaia Collaboration et al. 2016, 2023). The five brightest Gaia sources after HIP 65426 in this region (spanning separations of ∼17″–47″) have respective apparent G-band magnitudes of 11.98, 13.28, 14.12, 14.59, and 15.05. Their respective $G_{\rm BP} - G_{\rm RP}$ colors are 1.72, 0.72, 1.41, 1.47, and 1.32. HIP 65426 has no known stellar companions (Kouwenhoven et al. 2005; Chauvin et al. 2017; Petrus et al. 2021). Furthermore, the TESS Input Catalog (TIC; Stassun et al. 2018, 2019) gives a flux contamination ratio (i.e., ratio of the total contaminant flux within 210″ to HIP 65426's flux) of only 0.03 (see also Section 3.2). Overall, it is likely that significant signals in our TESS data correspond to HIP 65426.

3. Analysis

3.1. High-frequency δ Scuti Pulsations in HIP 65426

We calculated the amplitude spectrum of each TESS sector time series (Figure 1(abc)) using `lightkurve` (Lightkurve Collaboration et al. 2018) and identified several significant frequencies spanning ∼3–130 cycles day^{-1} (Figure 1(d)). For the high frequencies, we used `SigSpec` (Reegen 2007) to iteratively fit sine waves to the data above 10 cycles day^{-1}, and up to a spectral significance threshold of 10 (following, e.g., Gruberbauer et al. 2007; Zwintz et al. 2009; Sepulveda et al. 2022). This resulted in 13 significant pulsation frequencies for Sector 11 and 14 significant pulsation frequencies for Sectors 38 and 64. The pulsation frequencies span 28–131 cycles day^{-1}, consistent with pressure modes of δ Scuti stars (e.g., Kurtz 2022), and they are tabulated in Appendix A.

Figure 2(a) shows HIP 65426 in a Gaia DR3 (Gaia Collaboration et al. 2016, 2023) color–magnitude diagram (CMD) compared to the Kepler δ Scuti stars from Murphy et al. (2019) as well as the Kepler γ Doradus stars from Li et al. (2020). We created the CMD following the procedure described in Sepulveda et al. (2022), which includes corrections for extinction and reddening for the Kepler stars. We used $A_V = 0.038$ mag (Chen et al. 2012) for HIP 65426. The $G_{\rm BP} - G_{\rm RP}$ color and absolute G magnitude of HIP 65426 are consistent with the population of δ Scuti stars from the Kepler Mission (Figure 2(a)) as well as with the population of high-frequency δ Scuti stars recently detected in the Pleiades open cluster with TESS (Bedding et al. 2023).

We attempted an asteroseismic mode identification for HIP 65426 by constraining the large-frequency separation ($\Delta\nu$), which is a parameter that can also constrain the mean stellar density (Aerts et al. 2010). We used the `echelle` package (Hey & Ball 2020) to iterate through a range of trial $\Delta\nu$ values (5–9 cycles day^{-1}, which generously encompasses typical $\Delta\nu$ values, e.g., Bedding et al. 2020; Murphy et al. 2023) and visually inspected the échelle diagrams for regular vertical sequences following Bedding et al. (2020). We arrived at a possible value of $\Delta\nu = 7.23 \pm 0.02$ cycles day^{-1} (Figure 2(b)). This is consistent within the range that Bedding et al. (2020) found for their sample of high-frequency δ Scuti stars, but the resulting ridge patterns of HIP 65426 are too complex to confidently identify the majority of the pulsation modes. The rapid stellar rotation period (indicated by $v \sin i$ and our analysis in Section 3.2) greatly contributes to the complication (e.g., Reese 2022; Aerts & Tkachenko 2023, and references therein). Detailed asteroseismic modeling, which may yield an independent age estimate, is beyond the scope of this study.

We checked the TESS data for pulsation timing variations that could be caused by mutual gravitation with an orbital companion (e.g., Hey et al. 2020). Such effects would manifest as a periodic (or coherent) variation of the phase of all the δ Scuti pressure modes, and is only measurable for sufficiently massive planets on long enough periods (e.g., Murphy et al. 2016; Hey et al. 2021). However, if no variation is detected, it is possible to instead place an upper limit on the mass of the orbital companion known a priori to exist. This is also a useful tool to rule out stellar mass companions. We follow the same methodology as Hey et al. (2021) to place a dynamical mass upper limit on HIP 65426 b in the absence of coherent phase variations, using our posterior predictions of the orbit from Section 3.4. This results in a 95% upper limit of 12.8 $M_{\rm Jup}$,

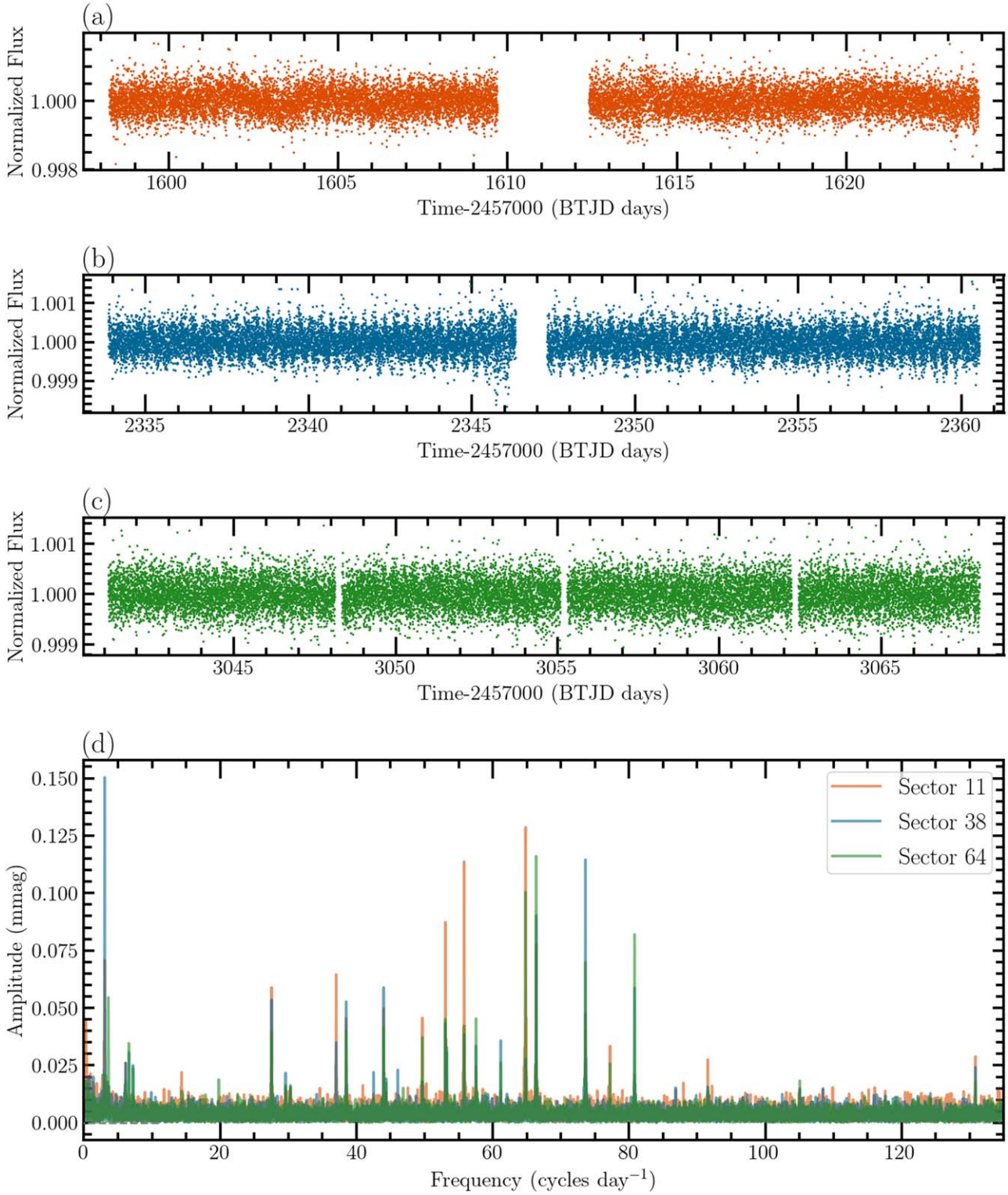

Figure 1. (a)–(c): TESS time-series photometry of HIP 65426 for Sectors 11, 38, and 64. (d): Amplitude spectra of each TESS sector in linear-linear space.

which serves as an independent verification that HIP 65426 b is likely in the giant planet mass regime. The 99.7% upper limit is 19.1 $M_{\rm Jup}$.

3.2. Rapid Differential Rotation in HIP 65426

Inspection of the <10 cycles day^{-1} region of the amplitude spectrum reveals several significant signals that are well-separated from the pressure modes (Figure 3). We identify two rotation frequencies, $f_{r,1} = 3.06$ cycles day^{-1} and $f_{r,2} = 3.60$ cycles day^{-1}. $f_{r,1}$ is detected in all three TESS sectors whereas $f_{r,2}$ is detected is only Sector 64. Gaussian functions were fit to the highest peak of each frequency and the best-fitting standard deviation is the reported uncertainty (Table 1). In the case of $f_{r,1}$, our adopted value is the average of the three separate detections from each

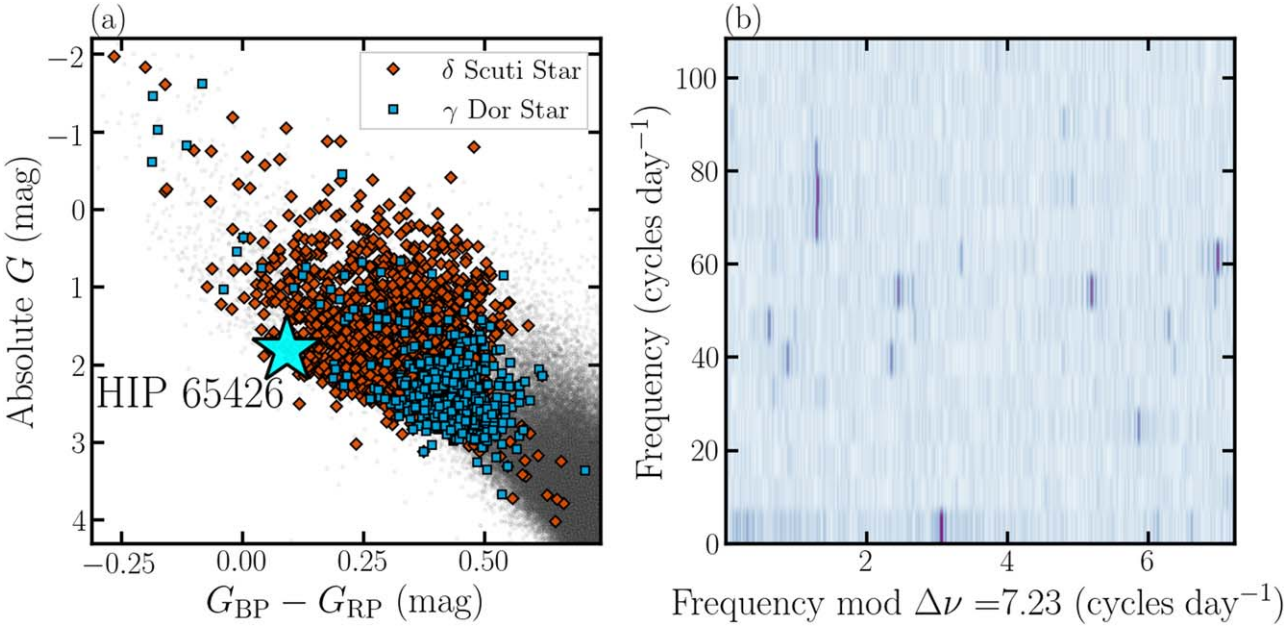

Figure 2. (a) Gaia color–magnitude diagram for a sample of Kepler stars generated following Sepulveda et al. (2022). HIP 65426 is overplotted as a large cyan star. The orange diamonds are the δ Scuti stars, blue squares are the γ Dor stars, and the small, gray, semitransparent dots are the general population of Kepler stars. (b): échelle diagram for HIP 65426 generated using our suggested large-frequency separation of $\Delta\nu = 7.23$ cycles day^{-1}. This plot uses an amplitude spectrum calculated from the concatenated TESS time series.

TESS sector. This yielded $f_{r,1} = 3.06 \pm 0.03$ cycles day^{-1} (7.85 ± 0.08 hr) and $f_{r,2} = 3.60 \pm 0.02$ cycles day^{-1} (6.67 ± 0.04 hr). We note that $2 \times f_{r,2}$ is similar to our estimated value for $\Delta\nu$. This is likely a coincidence, but supports the conclusion that rapid rotation will complicate the mode identification for this star.

We associated these signals with the stellar rotation period for the following reasons. Balona (2017) compared Kepler photometric rotation frequencies for a sample of 30 hot (8300–12,000 K) stars with their corresponding $v \sin i$ values and found that they correlated in a manner physically consistent with rotation frequencies. We overplotted $f_{r,1}$ and $f_{r,2}$ compared with the $v \sin i$ value of HIP 65426 (280 km s^{-1}; Section 3.3) along with the sample presented in Balona (2017) in Figure 4. Both follow the expected trend, which validates our interpretation of the signals as tracers of the stellar rotation frequency. We considered if HIP 65426 could be a hybrid pulsator showing gravity modes in addition to pressure modes (e.g., Grigahcène et al. 2010). However, low-frequency gravity modes often appear in groups of several dense peaks (e.g., Li et al. 2020), as opposed to more narrow signals like in the case of HIP 65426. Moreover, the TESS amplitude spectra show signal at $2 \times f_{r,1}$ and $2 \times f_{r,2}$ (Figure 3) consistent with rotation harmonics and an untypical feature for pulsations (e.g., Uytterhoeven et al. 2011). The peak at $\approx$6.6 cycles day^{-1} is associated with rotation, but we do not include it in Table 1 due to the absence of a subharmonic. This is not uncommon for rotational modulation (e.g., Kawaler 2021) and could be caused by multiple spots located at different longitudes. The same is likely true for the $2 \times f_{r,2}$ frequency in Sector 38 without $f_{r,2}$.

Together, we interpret the detection of $f_{r,1}$ and $f_{r,2}$ as evidence for surface latitudinal differential rotation in HIP 65426. The physical consistency of both frequencies with $v \sin i$, as well as their proximity to one another, is consistent with the two frequencies tracing different stellar latitudes rotating at different velocities. Moreover, while each TESS sector is only $\sim$27 days, they are separated by $\sim$2 yr, which corroborates a picture of spot evolution occurring on those timescales. This would also explain why $f_{r,2}$ is only detected in one sector and why $f_{r,1}$ shows amplitude variations between sectors. This is consistent with Balona & Abedigamba (2016), who analyzed the photometric rotation frequency spread for a sample of 522 hot (7400–10,000 K) A and F stars and found that $\approx$60% of this sample was consistent with exhibiting differential rotation. Their analysis used Kepler light curves with a continuous time baseline of $\sim$4 yr, while only three sectors of TESS data are available for HIP 65426, limiting more detailed investigation.

We noted in Section 2 an absence of nearby comparatively bright sources to HIP 65426, as well as a lack of stellar companions. We further assessed the likelihood that our reported rotation frequencies correspond to HIP 65426 and not a faint contaminating background source in the TESS aperture. To this end, we used the `TESS_localize` package (Higgins & Bell 2023), which is an algorithm designed to identify the most likely Gaia source in the TESS aperture responsible for producing a set of input frequencies. In very brief summary, the algorithm models the expected relative flux distribution of the input frequencies (i.e., the frequency amplitude) across TESS pixels to estimate the location of the variability source, assuming that only one source varies at the input frequencies. As an initial baseline, we began by running the routine to evaluate the three most significant pulsation frequencies of HIP 65426 (Table 2), separately for Sectors 11, 38, and 64, and down to a Gaia magnitude limit of 18. The corresponding per-sector relative probabilities that the pulsation frequencies correspond to HIP 65426 are respectively 97.9%, >99.9%, and >99.9%. We next ran the routine in the same manner but now to evaluate the rotation frequencies in each of the three TESS sectors (Table 1). The resulting relative probabilities that these rotation frequencies correspond to HIP 65426 are, respectively, 88.1%, >99.9%, and >99.9%. This evaluation contributes additional confidence that our

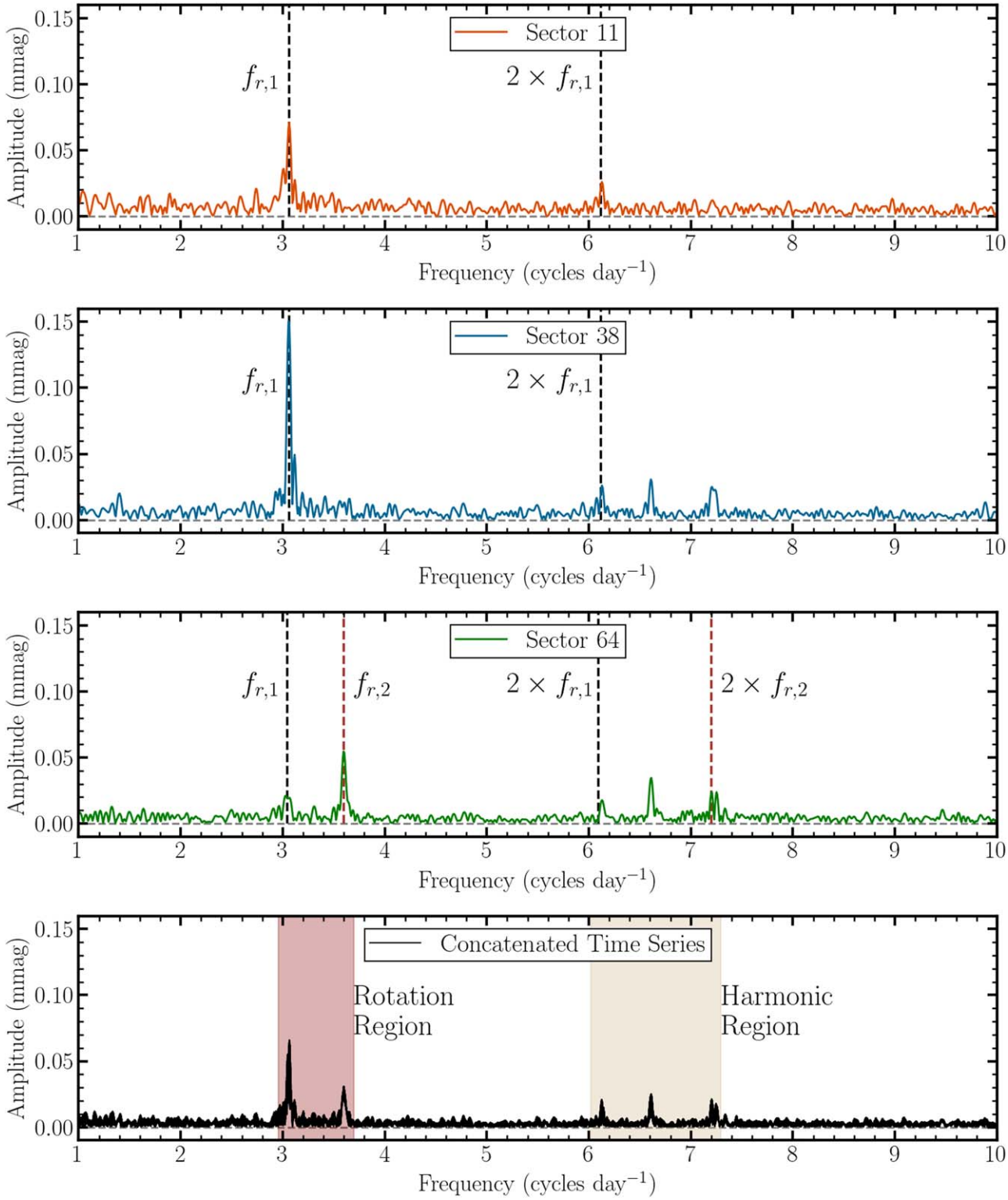

Figure 3. TESS amplitude spectra of HIP 65426, zoomed in on a region of low frequencies. Vertical dashed lines denote the locations of $f_{r,1}$, $f_{r,2}$ as described in Section 3.2, as well as the locations of $2 \times f_{r,1}$ and $2 \times f_{r,2}$.

TESS rotation frequencies (and pulsation frequencies) intrinsically correspond to HIP 65426.

3.3. HIP 65426 Stellar Inclination

We used our stellar rotation period together with published measurements of $v \sin i$ and stellar radius to constrain the stellar inclination. These parameters are related by a geometric relation (e.g., Doyle et al. 1984; Campbell & Garrison 1985):

$$i_\star = \sin^{-1}\left(\frac{v \sin i}{v}\right) = \sin^{-1}\left(\frac{v \sin i}{2\pi R_\star / P_{\rm rot}}\right). \quad (1)$$

Masuda & Winn (2020) noted that $v \sin i$ is not statistically independent of the rotational velocity, v (computed using $P_{\rm rot}$ and $R_\star$), and thus it is not appropriate to apply Monte Carlo

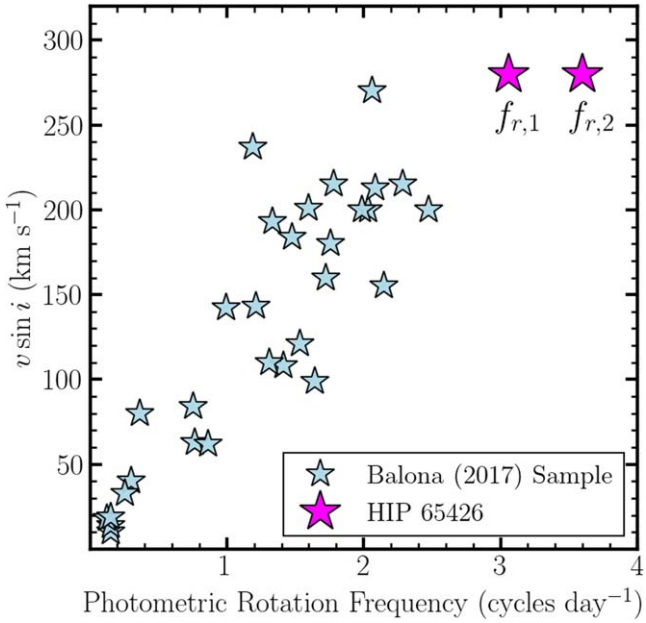

Figure 4. $v \sin i$ compared to photometric rotation frequency for the sample of hot (8300–12,000 K) stars presented in Balona (2017). Pink stars for HIP 65426 (8840 ± 200 K, Chauvin et al. 2017) are overplotted to represent both $f_{r,1}$ and $f_{r,2}$.

Table 1
TESS Rotation Frequencies of HIP 65426

	$f_{r,1}$ cycles day^{-1}	$P_{r,1}$ hr	$f_{r,2}$ cycles day^{-1}	$P_{r,2}$ hr
Sector 11	3.06 ± 0.02	7.84 ± 0.05	⋯	⋯
Sector 38	3.06 ± 0.02	7.84 ± 0.05	⋯	⋯
Sector 64	3.05 ± 0.04	7.87 ± 0.10	3.60 ± 0.02	6.67 ± 0.04
Adopted	3.06 ± 0.03	7.85 ± 0.08	3.60 ± 0.02	6.67 ± 0.04

Note. Equivalent rotation periods are included.

propagation of uncertainties. They provided a Bayesian framework that properly computes $\cos i$ given measurements of $P_{\rm rot}$, $R_\star$, and $v \sin i$. Bowler et al. (2023) expanded on this by deriving analytic expressions that approximate the framework of Masuda & Winn (2020) as long as $P_{\rm rot}$ is measured to $\lesssim$20%. We used the Bowler et al. (2023) expressions in this work to derive the inclination posterior of HIP 65426, $P(i_\star|P_{\rm rot}, R_\star, v \sin i)$. Their expressions (Equation (9) and (10); Bowler et al. 2023) assume uniform priors on the measured inputs, an isotropically uniform prior for $\cos i$, and Gaussian-distributed uncertainties on the inputs.

Chauvin et al. (2017) reported an isochrone-derived stellar radius of $R_\star = 1.77 \pm 0.05 R_\odot$, which is consistent with the TIC value of $R_\star = 1.74 \pm 0.05 R_\odot$ (Stassun et al. 2018, 2019) derived using the Stefan–Boltzmann law. As an input radius for HIP 65426, we used the mean of these two literature values. We note however that rapidly rotating intermediate mass stars are better described as oblate spheroids than spheres (e.g., van Belle et al. 2001; Domiciano de Souza et al. 2003; McAlister et al. 2005; Monnier et al. 2007). Therefore, HIP 65426 is likely not well described by a single radius but rather by a radius gradient that increases from polar to equatorial latitudes. HIP 65426 is too distant (i.e., its angular size is too small) to resolve with optical/infrared interferometry, a technique that can directly constrain the polar ($R_{\rm pol}$) and equatorial ($R_{\rm eq}$) radii for nearby stars with large projected angular sizes (e.g., van Belle 2012). To account for systematic uncertainty in our input radius due to unresolved oblateness, we consider $R_{\rm pol}$ and $R_{\rm eq}$ of Altair, a nearby δ Scuti star whose surface has been interferometrically resolved and who is of similar mass and rotational velocity as HIP 65426 (e.g., Buzasi et al. 2005; Monnier et al. 2007; Bouchaud et al. 2020). Using $R_{\rm pol} = 1.661 R_\odot$ and $R_{\rm eq} = 2.022 R_\odot$(Monnier et al. 2007) we calculate a fractional uncerainty of 10%, which we adopt for our input value for HIP 65426 (i.e., $R_\star = 1.76 \pm 0.18 R_\odot$).

For the input $v \sin i$, we used the mean of two reported values measured using HARPS spectroscopy: 299 ± 9 km s^{-1} (Chauvin et al. 2017) and 261 ± 2 km s^{-1} (Petrus et al. 2021). For the uncertainty, we used the standard error on the mean of the HARPS values, yielding 280 ± 13 km s^{-1}. We note that in the presence of latitudinal differential rotation, the spectroscopic $v \sin i$ (derived without accounting for differential rotation) will represent a weighted average of the set of latitudinal velocities and not soley represent the equatorial velocity. This is supported by interferometric imaging of the nearby A-star Altair, which has a $v \sin i$ of 241 km s^{-1} from detailed modeling (Monnier et al. 2007) and a $v \sin i$ from methods that ignore differential rotation of 216 km s^{-1} (mean Altair $v \sin i$ from: Bernacca & Perinotto 1970; Abt & Morrell 1995; Royer et al. 2002; Schröder et al. 2009). Detailed modeling of the differential rotation (and its effect on line broadening) in HIP 65426 is beyond the scope of this paper.

For the input rotation period, we took the mean of our two TESS rotation periods from Section 3.2. By taking the mean we appropriately match the weighted average velocity implied by the HARPS $v \sin i$ measurements. We opted to keep the larger of the two individual period uncertainties for our input mean period, i.e., 7.26 ± 0.08 hr.

The resulting posterior for $P(i_\star|P_{\rm rot}, R_\star, v \sin i)$ is shown in Figure 5. Here we have assumed a prograde orbit of HIP 65426 b relative to its host star, whereby the planet orbits clockwise on the sky (i.e., is inclined at $90° < i < 180°$; Section 3.4), and thus the inclination angle parameter space spans [90, 180]°. The posterior median and 68% credible interval is $i_\star = 107^{+12}_{-11}°$, with a maximum a posteriori of 107°. This indicates that HIP 65426 is most likely oriented somewhat edge-on, consistent with a priori expectation from the literature $v \sin i$ measurements. The 95% and 99.7% credible intervals span 91–127° and 90–133°, respectively.

3.4. HIP 65426 b Orbital Inclination

We conducted an orbit fit utilizing all the relative astrometry of HIP 65426 b available in the literature (Chauvin et al. 2017; Cheetham et al. 2019; Stolker et al. 2020; Carter et al. 2023), which includes three recently reported high-precision measurements with VLTI/GRAVITY (Blunt et al. 2023). Where multiple astrometric measurements from the same instrument and same night of observing are reported, we took their mean and treated them as a single epoch as follows. From Cheetham et al. (2019), we averaged the two SPHERE 2018.36 epochs into $[\rho, \theta] = [824.65 \pm 2.2$ mas, $149\overset{\circ}{.}87 \pm 0\overset{\circ}{.}16]$. From Carter et al. (2023), we averaged the two reported astrometric measurements from MIRI (2022.54) as well as five from NIRCam (2022.57) into two epochs, respectively $[\rho, \theta] = [829.5 \pm 13$ mas, $149 \pm 1°]$ and

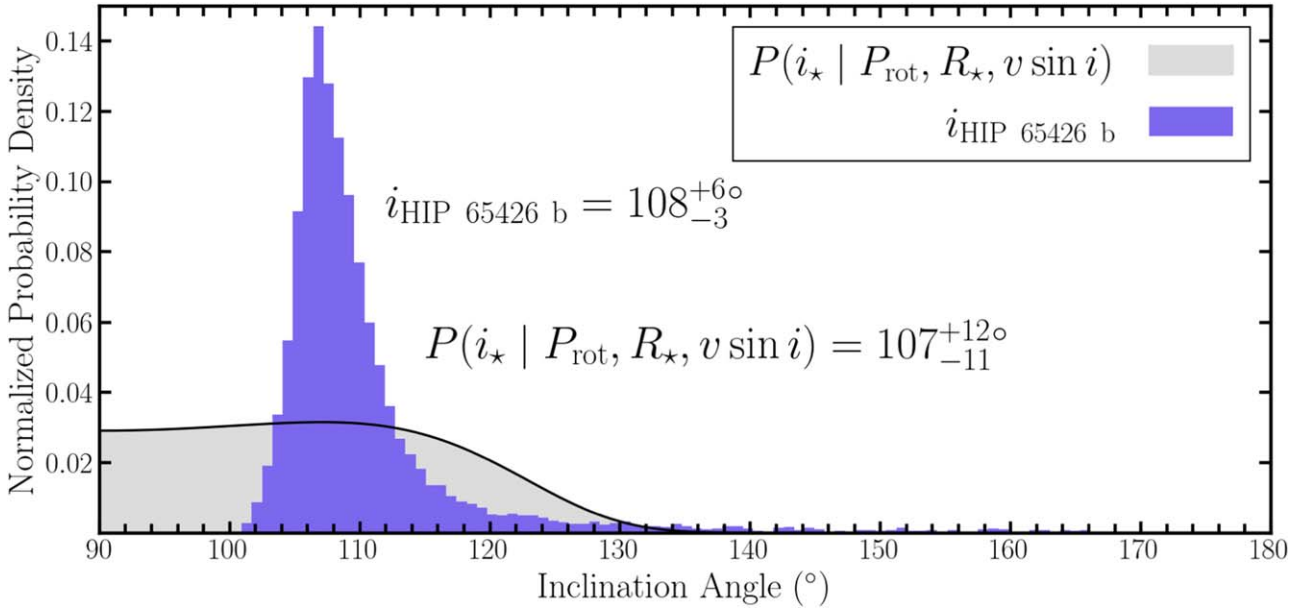

Figure 5. Normalized inclination posteriors for the HIP 65426 system, where $P(i_\star|P_{\rm rot}, R_\star, v \sin i)$ represents the host star rotational inclination and $i_{\rm HIP\ 65426\ b}$ represents the orbital inclination of HIP 65426 b. Median and 68% credible intervals are written in the figure.

$[\rho,\ \theta] = [819 \pm 6.2\,{\rm mas},\ 149\overset{\circ}{.}84 \pm 0\overset{\circ}{.}42]$. Stolker et al. (2020) reprocessed two NaCo epochs originally reported in Cheetham et al. (2019). We chose to use the values reported in Stolker et al. (2020), specifically using their final reported measurements after they applied their astrometric bias corrections. This in total amounts to 13 astrometric epochs spanning a ~7 yr baseline (2016.41–2023.35).

We considered inflating the astrometric uncertainties to account for potential systematics following the approach of some recent orbit-fitting studies with relative astrometry (Bowler et al. 2020; Sepulveda & Bowler 2022). In short, a linear model is assumed for ρ and θ as a function of time, and a reduced χ^2 (χ^2_ν) is calculated. For any astrometric measurements only reported in [ΔR.A.,ΔDecl.] form, we converted to $[\rho, \theta]$ in a Monte Carlo fashion. If χ^2_ν was greater than unity, we iteratively increased a "jitter" uncertainty term added in quadrature to the base uncertainty until χ^2_ν reaches unity. However, for the HIP 65426 b data set used in this study, χ^2_ν was already less than unity for both ρ and θ (respectively 0.4 and 0.3, with $\nu = 11$), which suggests that the uncertainties are likely reasonable and we thus incorporated no additional uncertainty. A summary figure is displayed as Figure 8.

We fitted Keplerian orbits to our astrometric data set using `orbitize!` (Blunt et al. 2020). We used `ptemcee` mode (Foreman-Mackey et al. 2013; Vousden et al. 2016), which utilizes the parallel-tempered affine-invariant ensemble sampler of Markov chain Monte Carlo (Goodman & Weare 2010). The varied parameters are standard for a Keplerian orbit with relative astrometry: a (semimajor axis), e (eccentricity), i (inclination), ω (argument of periastron of the planet's orbit), Ω (position angle of the ascending node), τ (time of last periapsis, as defined in Blunt et al. 2020 with $t_{\rm ref}$ =MJD 58849), ϖ (parallax), and $M_{\rm tot}$ (total mass of the system). We chose a Gaussian $M_{\rm tot}$ prior of $2.0 \pm 0.1\ M_\odot$, consistent with previous mass estimates of HIP 65426 (Tetzlaff et al. 2011; Chauvin et al. 2017; Bochanski et al. 2018). The ϖ prior was a Gaussian of 9.303 ± 0.035 mas from Gaia DR3 (Gaia Collaboration et al. 2016, 2023). The prior for a was log-uniform ranging from 1 to 500 au. For i we used an isotropic ($P(i) \propto \sin i$) prior ranging from 0–π rad. We use linearly uniform priors for the remaining parameters with ranges: 0–1 for e; 0–2π rad for ω and Ω; and 0–1 for τ. To assist convergence, we chose to initialize the walkers at positions near the best-fit values as guided from preliminary orbit fits that we conducted as well as from prior orbit fits in the literature (e.g., Blunt et al. 2023; Carter et al. 2023). We ran `ptemcee` with 1500 walkers, 18 temperatures, and for 1.6×10^5 steps per walker per temperature. A burn-in size of the first 50% of steps are removed, and we also apply a thinning factor of 20 to mitigate the effect of correlation. Keeping only the samples of the lowest temperature yields a final total of 6×10^6 posterior orbit samples. A sample of sky-projected posterior orbits are displayed as Figure 6, and a selection of posterior orbital elements are displayed in Appendix B.

The most important result for the purposes of our study is the orbital inclination posterior ($i_{\rm HIP\ 65426\ b}$), which is shown in Figure 5. The median and 68% credible interval is $108^{+6}_{-3}{}^\circ$; the 95% credible interval spans 103°–139°. Our inclination posterior is consistent within the 68% uncertainties to those of recent studies (e.g., Blunt et al. 2023; Carter et al. 2023; Do et al. 2023), despite minor differences in the choices of input astrometry and priors.

4. Discussion

4.1. A Lack of Evidence for Misalignment

The inclination posteriors for HIP 65426 b and its host star are compared in Figure 5. They are consistent within their 68% uncertainties, which we interpret as a lack of significant evidence for misalignment. In the absence of knowledge of the stellar rotation axis orientation, the best available proxy for the true star-planet obliquity is the inclination difference of HIP 65426 b and its host star, $|\Delta i| = |i_\star - i_{\rm HIP\ 65426\ b}|$, which represents a minimum inclination difference with respect to the true obliquity. We place 68% and 95% upper limits of $|\Delta i| < 13°$ and $|\Delta i| < 25°$, respectively, for the HIP 65426 system.

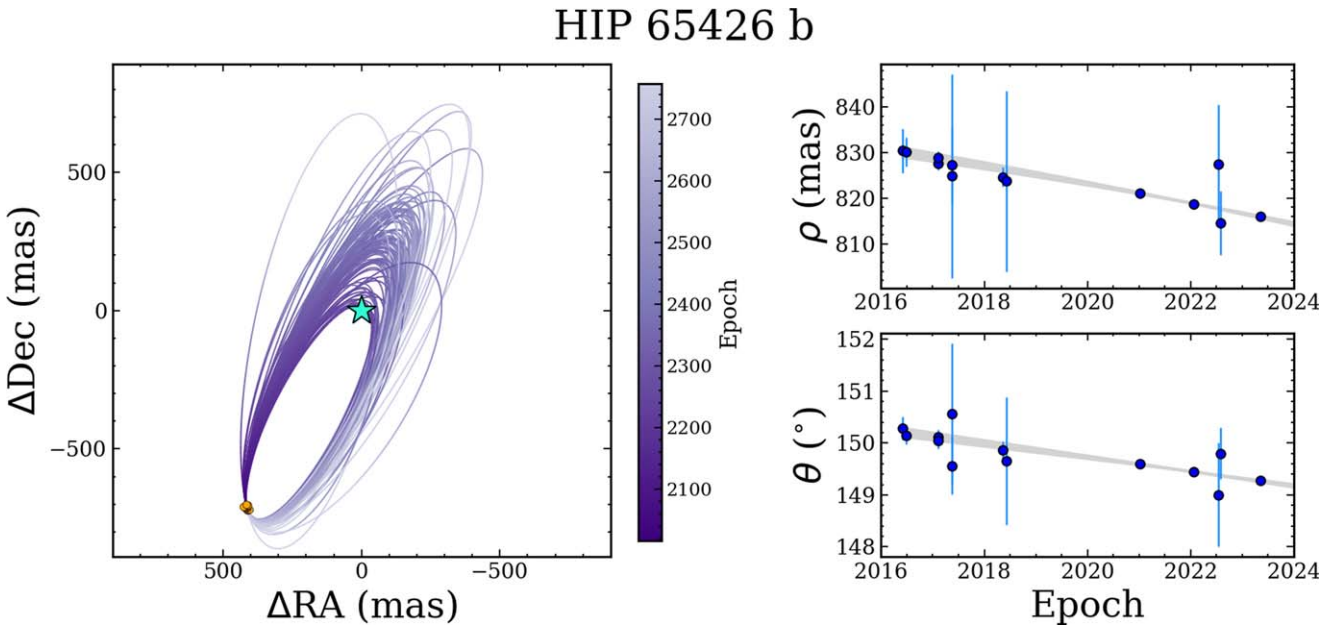

Figure 6. The left panel displays a sample of 100 sky-projected posterior orbits resulting from our fit of HIP 65426 b. The cyan star represents the position of HIP 65426 and the orange dots represent the relative astrometry of HIP 65426 b (with no error bars on this panel). The right panels compare the model orbit separation and position angles from the same 100 posterior orbits to the input astrometric data.

4.2. Formation of HIP 65426 b

The wide orbit of HIP 65426 b is particularly interesting with respect to its formation history because core accretion is not expected to operate efficiently at separations of several tens of au (e.g., Pollack et al. 1996; Dodson-Robinson et al. 2009; Rafikov 2011). Coupled with the large eccentricity implied by early orbit-fitting studies, planet–planet scattering has been proposed as a possible contributing mechanism for HIP 65426 b's presently observed orbit. Marleau et al. (2019) explored planet–planet scattering scenarios in detail using the system properties together with *N*-body modeling. If HIP 65426 b formed via core accretion at a location interior to its present-day orbit, Marleau et al. (2019) suggest the presence of additional yet-undetected interior planets that would have participated in gravitationally scattering HIP 65426 b. Our lack of significant evidence for misalignment stands to disfavor a core accretion followed-by planet–planet scattering scenario because the latter is generally expected to result in high mutual inclinations (Chatterjee et al. 2008; Ford & Rasio 2008). Although with incomplete geometric information, it is still possible that the true obliquity of HIP 65426 could be larger than $|\Delta i|$.

It is important to note that the orbital eccentricity of HIP 65426 b, which has played a key role in preliminary interpretations of its history, is not yet concretely determined. The most recent orbit fit by Blunt et al. (2023) using high-precision astrometry from VLTI/GRAVITY (as well as this work, which incorporated their GRAVITY data) disfavor the largest orbital eccentricities that were previously plausible based on eccentricity posteriors from earlier studies. Blunt et al. (2023) also showed that even with three GRAVITY epochs, the choice of eccentricity prior still influences the posterior. Do et al. (2023) previously demonstrated this as well, where their adoption of an observable-based eccentricity prior (O'Neil et al. 2019) yielded an eccentricity posterior for HIP 65426 b more consistent with lower eccentricities compared to that derived with a uniform eccentricity prior. Continued astrometric monitoring to determine an accurate orbital eccentricity that is prior-independent will be needed to better understand the formation of HIP 65426 b.

4.3. Trends for Directly Imaged Giant Planets

The lack of evidence for misalignment for HIP 65426 b furthers an emerging trend where imaged long-period giant planets appear preferentially aligned with their host stars (Bowler et al. 2023). We illustrate this in Figure 7 where orbital inclinations and host star inclinations are compared for 6 directly imaged exoplanet systems comprising 11 total companions: HR 8799 bcde (Marois et al. 2008, 2010), 51 Eri b (De Rosa et al. 2015; Macintosh et al. 2015), PDS 70 bc (Keppler et al. 2018; Haffert et al. 2019; Mesa et al. 2019), β Pic bc (Lagrange et al. 2009, 2010, 2019; Nowak et al. 2020), AF Lep b (De Rosa et al. 2023; Franson et al. 2023; Mesa et al. 2023), and HIP 65426 b (Chauvin et al. 2017). The stellar and orbital inclination references are as follows: HR 8799 (Sepulveda & Bowler 2022; Sepulveda et al. 2023), 51 Eri (Dupuy et al. 2022; Bowler et al. 2023), PDS 70 (Wang et al. 2021; Bowler et al. 2023), β Pic (Zwintz et al. 2019; Brandt et al. 2021), AF Lep (Zhang et al. 2023), and HIP 65426 (this work). We use median values (or alternatively maximum a posteriori values if no median is reported) and 68% uncertainties to represent the error bars. For β Pic,[7] no uncertainty is reported on the asteroseismic stellar inclination estimate from Zwintz et al. (2019), and we thus adopted a 10% uncertainty. The imaged giant planet sample in Figure 7 are all unambiguously consistent with $|\Delta i| < 10°$, provided the adopted inclination uncertainties.

[7] β Pictoris is a rare exception among directly imaged exoplanet systems where the full obliquity has been constrained. The proximity of β Pictoris enabled Kraus et al. (2020) to interferometrically determine the sky-projected position angle of its equator. Together with the asteroseismic stellar inclination from Zwintz et al. (2019) Kraus et al. (2020) determined a true mutual inclination angle of $\leqslant 3 \pm 5°$ for β Pic b and its host star.

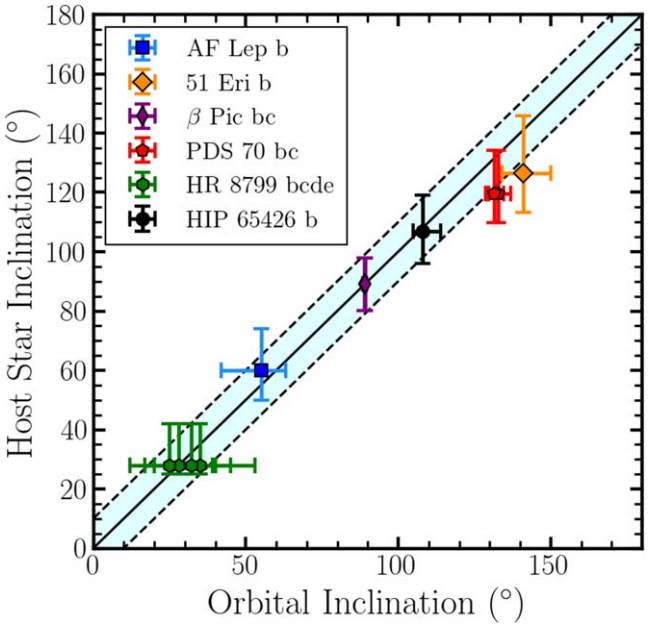

Figure 7. Orbital inclination compared to stellar inclination for a sample of six directly imaged exoplanet systems (comprising 11 total planets) assuming prograde orbits with respect to the host star. The solid black line denotes the 1:1 relation, and the light cyan region bordered by dashed black lines encapsulates an inclination difference $\pm 10°$ of the black line. References for the inclination angles are given in Section 4.3.

Dusty debris disks, which represent extrasolar Kuiper Belt analogs (e.g., Hughes et al. 2018; Marino 2022, and references therein), were also shown to be preferentially aligned with their host stars based on early studies with small ($N = 8$–10) sample sizes (Watson et al. 2011; Greaves et al. 2014). Recently, Hurt & MacGregor (2023) evaluated $|\Delta i|$ for a larger sample size of 31 debris disk systems. While they found some examples of significantly misaligned systems, the lack of significant evidence for misalignment persisted in $\gtrsim$80% of their sample, which still suggests that most debris disks are preferentially aligned with their host stars. Additional observations will show whether the link in the formation and dynamical evolution of imaged giant planets and debris disks continues to hold for obliquities.

If this trend does hold true for imaged giant planets, it would contrast with the emerging obliquity trends found for imaged brown dwarfs, which imply that misalignments are common (Bowler et al. 2023). Together with distinctions in other fundamental properties (e.g., underlying orbital eccentricity distributions; Bowler et al. 2020; Do et al. 2023; Nagpal et al. 2023) this could be further illustrating brown dwarfs and giant planets as distinct classes of objects with differing formation pathways. Future direct imaging discoveries that can include a TESS analysis of the host star will help to create a larger and more diverse sample size to determine whether this population-level obliquity trend for imaged giant planets holds true.

5. Conclusion

We analyzed TESS time-series photometry of the directly imaged exoplanet host star HIP 65426. We detected several pulsation modes consistent with classification as a high-frequency δ Scuti pulsator. We find a preliminary estimate of $\Delta\nu = 7.23 \pm 0.02$ cycles day^{-1}, consistent with other young δ Scuti stars (Bedding et al. 2020). We also used the nondetection of pulsation timing variations to estimate a 95% dynamical mass upper limit of 12.8 $M_{\rm Jup}$ for HIP 65426 b, independently supporting its planetary mass.

From the TESS data we also detected rapid photometric rotation frequencies of 7.85 ± 0.08 hr and 6.67 ± 0.04 hr that we interpreted as evidence of latitudinal differential rotation in HIP 65426. Using published radius and $v \sin i$ constraints together with our TESS rotation frequencies, we jointly measured the inclination of HIP 65426 to $i_\star = 107^{+12}_{-11}°$. This near edge-on inclination of the host star is consistent with HIP 65426 b's near edge-on inclination of $108^{+6}_{-3}°$ that we determined from our orbit fit of the available relative astrometry. We thus found no significant evidence for spin–orbit misalignment in the HIP 65426 system. This finding further supports an emerging trend of preferential alignment between imaged long-period giant planets and their host stars (Figure 7), which is similar to the emerging trend for debris disks and dissimilar to that for imaged brown dwarfs.

This work adds to the synergy of using space-based photometric data and direct imaging data to probe the *outer* architectures of extrasolar systems at an epoch after planet formation has occurred. Evaluating the time-series photometry of additional host stars of imaged exoplanet, brown dwarf, and debris disk systems will be key to investigating the emerging obliquity trends. Likewise, dedicated missions and surveys to discover new systems and robustly characterize the inclinations of their constituents will also be a complementary necessity.

Acknowledgments

A.G.S thanks Brendan P. Bowler and Sarah Blunt for collaborative discussions that helped expedite this work, as well as Mitchell T. Dennis for assistance with operating the HPC clusters Mana and Koa.

This material is based upon work supported by the National Science Foundation Graduate Research Fellowship Program under grant No. 1842402 and 2236415. D.H. acknowledges support from the Alfred P. Sloan Foundation, the National Aeronautics and Space Administration (80NSSC21K0784), and the Australian Research Council (FT200100871).

This work has benefitted from The UltracoolSheet (Best et al. 2020), maintained by Will Best, Trent Dupuy, Michael Liu, Rob Siverd, and Zhoujian Zhang, and developed from compilations by Dupuy & Liu (2012), Dupuy & Kraus (2013), Liu et al. (2016), Best et al. (2018), and Best et al. (2021).

The technical support and advanced computing resources from University of Hawaii Information Technology Services—Cyberinfrastructure, funded in part by the National Science Foundation MRI award # 1920304, are gratefully acknowledged.

This paper includes data collected by the TESS mission, which are publicly available from the Mikulski Archive for Space Telescopes (MAST). Funding for the TESS mission is provided by the NASA's Science Mission Directorate.

This work has made use of data from the European Space Agency (ESA) mission Gaia (https://www.cosmos.esa.int/gaia), processed by the Gaia Data Processing and Analysis Consortium (DPAC; https://www.cosmos.esa.int/web/gaia/dpac/consortium). Funding for the DPAC has been provided by national institutions, in particular the institutions participating in the Gaia Multilateral Agreement.

This research has made use of the VizieR catalog access tool, CDS, Strasbourg, France. The original description of the VizieR service was published in Ochsenbein et al. (2000).

This research has made use of the SIMBAD database, operated at CDS, Strasbourg, France.

This research has made use of NASA's Astrophysics Data System Bibliographic Services.

Facility: TESS

Software: `lightkurve` (Lightkurve Collaboration et al. 2018), `SigSpec` (Reegen 2007), `echelle` (Hey & Ball 2020), `orbitize!` (Blunt et al. 2020), `ptemcee` (Foreman-Mackey et al. 2013; Vousden et al. 2016), `TESS_localize` (Higgins & Bell 2023), `matplotlib` (Hunter 2007), `astropy` (Astropy Collaboration et al. 2013, 2018), `numpy` (Harris et al. 2020), `scipy` (Virtanen et al. 2020), `astroquery` (Ginsburg et al. 2019)

Appendix A
HIP 65426 Pulsation Frequencies

Here we tabulate the HIP 65426 pulsation frequencies that we extracted from each sector of TESS photometry (Table 2). We report the cumulative spectral significance and Fourier-domain phase angles as defined in Reegen (2011). Uncertainties were calculated following Kallinger et al. (2008).

Table 2
Significant Pulsation Frequencies of HIP 65426 from TESS Photometry

Frequency (cycles day^{-1})	Amplitude (mmag)	Phase Angle (rads)	Spectral Significance
Sector 11			
27.547 ± 0.006	0.059 ± 0.009	−2.58 ± 0.07	46
37.029 ± 0.005	0.066 ± 0.009	−2.15 ± 0.06	56
38.499 ± 0.007	0.045 ± 0.009	−0.73 ± 0.09	28
43.995 ± 0.007	0.050 ± 0.009	−2.64 ± 0.08	33
49.664 ± 0.007	0.045 ± 0.009	0.03 ± 0.09	28
53.060 ± 0.004	0.089 ± 0.009	−1.43 ± 0.05	98
55.800 ± 0.003	0.114 ± 0.009	1.62 ± 0.04	153
64.821 ± 0.003	0.129 ± 0.009	1.64 ± 0.03	185
66.363 ± 0.004	0.077 ± 0.009	−0.32 ± 0.05	75
73.606 ± 0.007	0.047 ± 0.009	0.82 ± 0.08	30
77.21 ± 0.01	0.034 ± 0.009	2.7 ± 0.1	16
91.56 ± 0.01	0.028 ± 0.008	1.0 ± 0.1	11
130.83 ± 0.01	0.029 ± 0.009	0.3 ± 0.1	12
Sector 38			
27.550 ± 0.005	0.054 ± 0.008	−2.63 ± 0.07	50
37.028 ± 0.008	0.036 ± 0.007	−0.4 ± 0.1	23
38.502 ± 0.005	0.053 ± 0.008	−2.17 ± 0.07	49
43.996 ± 0.005	0.060 ± 0.008	−0.57 ± 0.06	60
53.059 ± 0.006	0.044 ± 0.008	0.11 ± 0.08	34
53.26 ± 0.01	0.028 ± 0.007	−1.0 ± 0.1	14
55.801 ± 0.007	0.038 ± 0.008	0.33 ± 0.09	26
57.550 ± 0.008	0.034 ± 0.007	1.5 ± 0.1	21
61.182 ± 0.008	0.036 ± 0.008	3.1 ± 0.1	23
64.82 ± 0.01	0.027 ± 0.007	1.0 ± 0.1	13
66.363 ± 0.003	0.090 ± 0.008	−1.45 ± 0.04	130
73.604 ± 0.003	0.116 ± 0.008	0.38 ± 0.03	206
80.814 ± 0.005	0.059 ± 0.008	2.25 ± 0.06	58
130.84 ± 0.01	0.024 ± 0.007	−0.6 ± 0.1	11
Sector 64			
27.550 ± 0.006	0.036 ± 0.006	0.35 ± 0.08	36
38.507 ± 0.006	0.036 ± 0.006	2.10 ± 0.08	38
44.001 ± 0.006	0.038 ± 0.006	1.20 ± 0.07	39
49.663 ± 0.007	0.034 ± 0.006	−1.23 ± 0.08	32
53.052 ± 0.006	0.054 ± 0.008	1.02 ± 0.07	45
53.266 ± 0.007	0.028 ± 0.005	2.67 ± 0.09	26
55.793 ± 0.006	0.044 ± 0.007	0.33 ± 0.07	42
57.549 ± 0.005	0.053 ± 0.008	−3.10 ± 0.07	45
61.18 ± 0.01	0.027 ± 0.007	−0.4 ± 0.1	17
64.821 ± 0.003	0.090 ± 0.006	−2.56 ± 0.03	193
66.363 ± 0.002	0.116 ± 0.007	1.92 ± 0.03	257
73.604 ± 0.004	0.059 ± 0.006	−2.66 ± 0.05	105
77.21 ± 0.01	0.024 ± 0.006	1.8 ± 0.1	15
80.811 ± 0.003	0.060 ± 0.005	−1.45 ± 0.04	139

Appendix B
HIP 65426 b Orbit Fit

Here we display the relative astrometry used in our orbit fit along with the best-fitting linear models used to evaluate the astrometric uncertainties (Figure 8). The 1D marginalized posterior distribution for a selection of orbital parameters are displayed in Figure 9. The orbital period (P) posterior is generated using our a and $M_{\rm tot}$ posterior samples and applying Kepler's Third Law in a Monte Carlo fashion. We note that our posterior for $M_{\rm tot}$, which is not displayed in Figure 9, is unconstrained by the astrometric data and merely recovers our prior probability choice.

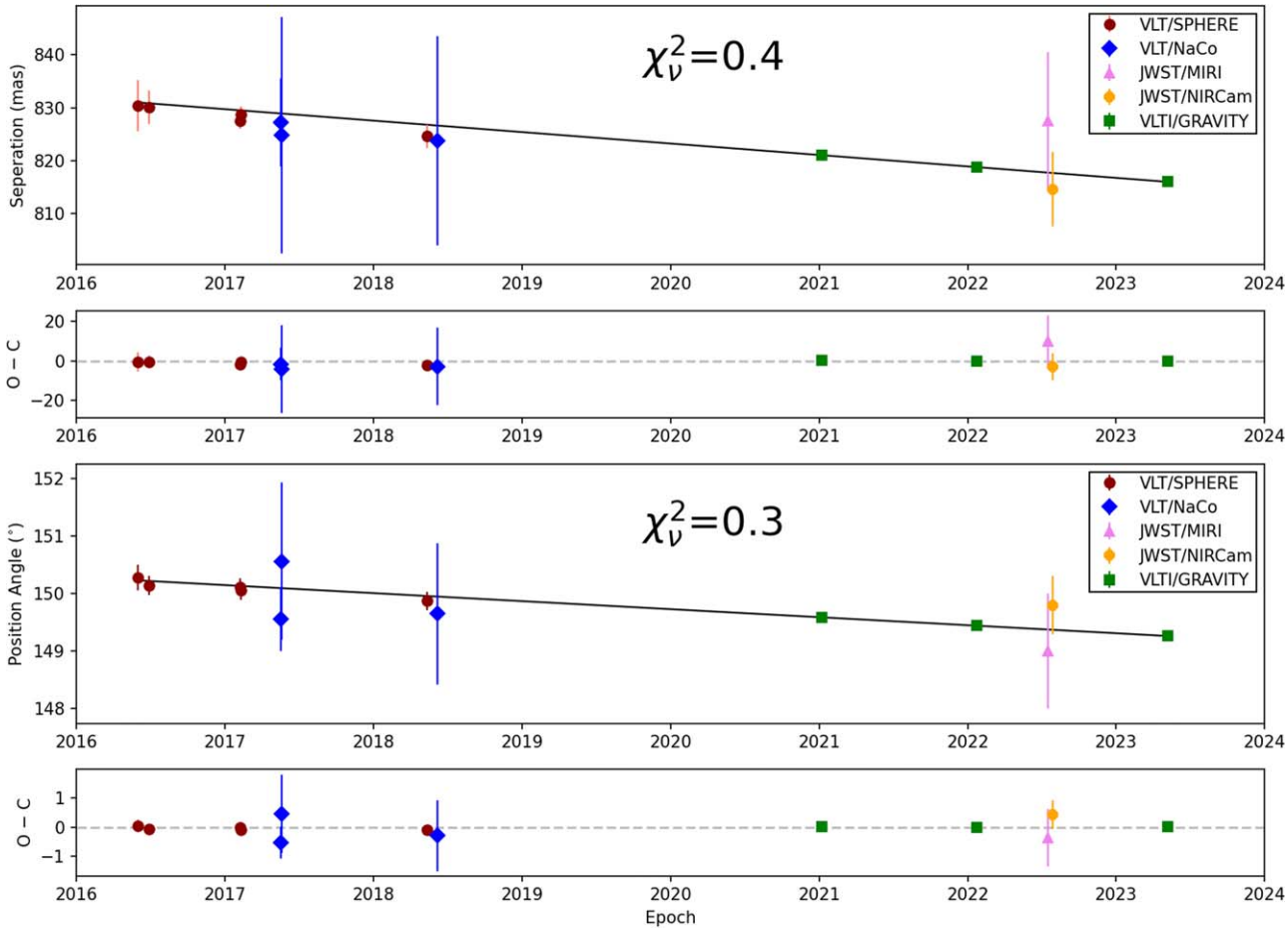

Figure 8. Relative astrometry of HIP 65426 b used in our orbit fit (Section 3.4) compared to our best-fitting linear models used to evaluate the astrometric uncertainties. Even with the inclusion of high-precision measurements from GRAVITY, the uncertainties overall appear reasonable.

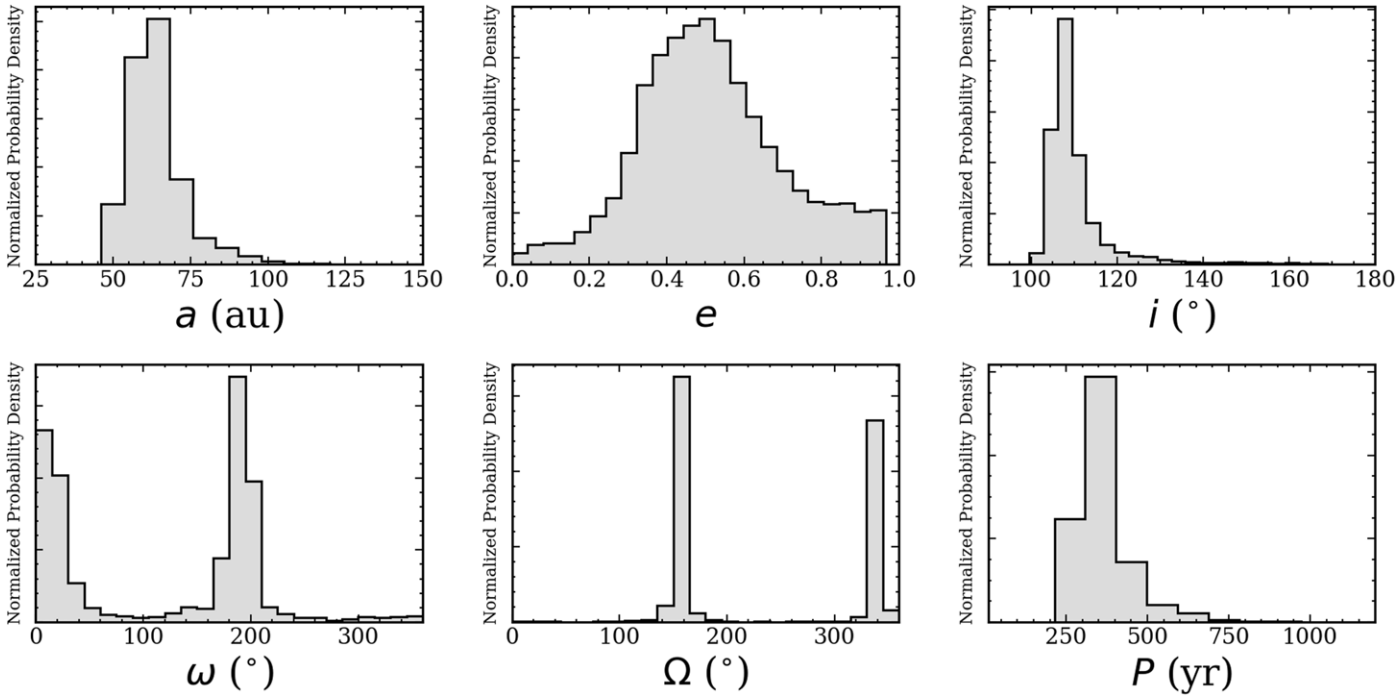

Figure 9. 1D posterior probability densities from our orbit fit of HIP 65426 b.

ORCID iDs

Aldo G. Sepulveda https://orcid.org/0000-0002-8621-2682
Daniel Huber https://orcid.org/0000-0001-8832-4488
Timothy R. Bedding https://orcid.org/0000-0001-5222-4661
Daniel R. Hey https://orcid.org/0000-0003-3244-5357
Simon J. Murphy https://orcid.org/0000-0002-5648-3107
Zhoujian Zhang https://orcid.org/0000-0002-3726-4881
Michael C. Liu https://orcid.org/0000-0003-2232-7664

References

Abt, H. A., & Morrell, N. I. 1995, ApJS, 99, 135
Aerts, C., Christensen-Dalsgaard, J., & Kurtz, D. W. 2010, Asteroseismology (Berlin: Springer)
Aerts, C., & Tkachenko, A. 2023, arXiv:2311.08453
Affer, L., Micela, G., Favata, F., & Flaccomio, E. 2012, MNRAS, 424, 11
Albrecht, S. H., Dawson, R. I., & Winn, J. N. 2022, PASP, 134, 082001
Astropy Collaboration, Price-Whelan, A. M., Sipőcz, B. M., et al. 2018, AJ, 156, 123
Astropy Collaboration, Robitaille, T. P., Tollerud, E. J., et al. 2013, A&A, 558, A33
Balona, L. A. 2011, MNRAS, 415, 1691
Balona, L. A. 2013, MNRAS, 431, 2240
Balona, L. A. 2017, MNRAS, 467, 1830
Balona, L. A., & Abedigamba, O. P. 2016, MNRAS, 461, 497
Bedding, T. R., Murphy, S. J., Crawford, C., et al. 2023, ApJL, 946, L10
Bedding, T. R., Murphy, S. J., Hey, D. R., et al. 2020, Natur, 581, 147
Bernacca, P. L., & Perinotto, M. 1970, Contributi dell'Osservatorio Astrofisica dell'Universita di Padova in Asiago, 239, 1
Best, W. M. J., Dupuy, T. J., Liu, M. C., Siverd, R. J., & Zhang, Z. 2020, The UltracoolSheet: Photometry, Astrometry, Spectroscopy, and Multiplicity for 3000+ Ultracool Dwarfs and Imaged Exoplanets, v1.0.0, Zenodo, doi:10.5281/zenodo.4169085
Best, W. M. J., Liu, M. C., Magnier, E. A., & Dupuy, T. J. 2021, AJ, 161, 42
Best, W. M. J., Magnier, E. A., Liu, M. C., et al. 2018, ApJS, 234, 1
Blunt, S., Balmer, W. O., Wang, J. J., et al. 2023, AJ, 166, 257
Blunt, S., Wang, J. J., Angelo, I., et al. 2020, AJ, 159, 89
Bochanski, J. J., Faherty, J. K., Gagné, J., et al. 2018, AJ, 155, 149
Bouchaud, K., Domiciano de Souza, A., Rieutord, M., Reese, D. R., & Kervella, P. 2020, A&A, 633, A78
Bowler, B. P., Blunt, S. C., & Nielsen, E. L. 2020, AJ, 159, 63
Bowler, B. P., Kraus, A. L., Bryan, M. L., et al. 2017, AJ, 154, 165
Bowler, B. P., Tran, Q. H., Zhang, Z., et al. 2023, AJ, 165, 164
Brandt, G. M., Brandt, T. D., Dupuy, T. J., Li, Y., & Michalik, D. 2021, AJ, 161, 179
Bryan, M. L., Chiang, E., Bowler, B. P., et al. 2020, AJ, 159, 181
Buzasi, D. L., Bruntt, H., Bedding, T. R., et al. 2005, ApJ, 619, 1072
Campbell, B., & Garrison, R. F. 1985, PASP, 97, 180
Carter, A. L., Hinkley, S., Kammerer, J., et al. 2023, ApJL, 951, L20
Chatterjee, S., Ford, E. B., Matsumura, S., & Rasio, F. A. 2008, ApJ, 686, 580
Chauvin, G., Desidera, S., Lagrange, A. M., et al. 2017, A&A, 605, L9
Cheetham, A. C., Samland, M., Brems, S. S., et al. 2019, A&A, 622, A80
Chen, C. H., Pecaut, M., Mamajek, E. E., Su, K. Y. L., & Bitner, M. 2012, ApJ, 756, 133
De Rosa, R. J., Nielsen, E. L., Blunt, S. C., et al. 2015, ApJL, 814, L3
De Rosa, R. J., Nielsen, E. L., Wahhaj, Z., et al. 2023, A&A, 672, A94
de Zeeuw, P. T., Hoogerwerf, R., de Bruijne, J. H. J., Brown, A. G. A., & Blaauw, A. 1999, AJ, 117, 354
Do Ó, C. R., O'Neil, K. K., Konopacky, Q. M., et al. 2023, AJ, 166, 48
Dodson-Robinson, S. E., Veras, D., Ford, E. B., & Beichman, C. A. 2009, ApJ, 707, 79
Domiciano de Souza, A., Kervella, P., Jankov, S., et al. 2003, A&A, 407, L47
Doyle, L. R., Wilcox, T. J., & Lorre, J. J. 1984, ApJ, 287, 307
Dupuy, T. J., Brandt, G. M., & Brandt, T. D. 2022, MNRAS, 509, 4411
Dupuy, T. J., & Kraus, A. L. 2013, Sci, 341, 1492
Dupuy, T. J., & Liu, M. C. 2012, ApJS, 201, 19
Ford, E. B., & Rasio, F. A. 2008, ApJ, 686, 621
Foreman-Mackey, D., Hogg, D. W., Lang, D., & Goodman, J. 2013, PASP, 125, 306
Franson, K., Bowler, B. P., Zhou, Y., et al. 2023, ApJL, 950, L19
Gaia Collaboration, Brown, A. G. A., Vallenari, A., et al. 2021, A&A, 649, A1
Gaia Collaboration, Prusti, T., de Bruijne, J. H. J., et al. 2016, A&A, 595, A1
Gaia Collaboration, Vallenari, A., Brown, A. G. A., et al. 2023, A&A, 674, A1
Gardner, J. P., Mather, J. C., Abbott, R., et al. 2023, PASP, 135, 068001
Gardner, J. P., Mather, J. C., Clampin, M., et al. 2006, SSRv, 123, 485
Ginsburg, A., Sipőcz, B. M., Brasseur, C. E., et al. 2019, AJ, 157, 98
Goodman, J., & Weare, J. 2010, Commun. Appl. Math. Comput. Sci., 5, 65
Grandjean, A., Lagrange, A. M., Keppler, M., et al. 2020, A&A, 633, A44
Greaves, J. S., Kennedy, G. M., Thureau, N., et al. 2014, MNRAS, 438, L31
Grigahcène, A., Antoci, V., Balona, L., et al. 2010, ApJL, 713, L192
Gruberbauer, M., Kolenberg, K., Rowe, J. F., et al. 2007, MNRAS, 379, 1498

Haffert, S. Y., Bohn, A. J., de Boer, J., et al. 2019, NatAs, 3, 749
Harris, C. R., Millman, K. J., van der Walt, S. J., et al. 2020, Natur, 585, 357
Hey, D., & Ball, W. 2020, Echelle: Dynamic echelle diagrams for asteroseismology, v1.4, Zenodo, doi:10.5281/zenodo.3629933
Hey, D. R., Montet, B. T., Pope, B. J. S., Murphy, S. J., & Bedding, T. R. 2021, AJ, 162, 204
Hey, D. R., Murphy, S. J., Foreman-Mackey, D., et al. 2020, AJ, 159, 202
Higgins, M. E., & Bell, K. J. 2023, AJ, 165, 141
Hinkley, S., Carter, A. L., Ray, S., et al. 2022, PASP, 134, 095003
Houk, N. 1978, Michigan catalog of two-dimensional spectral types for the HD stars (Ann Arbor, MI: Univ. of Michigan)
Hughes, A. M., Duchêne, G., & Matthews, B. C. 2018, ARA&A, 56, 541
Hunter, J. D. 2007, CSE, 9, 90
Hurt, S. A., & MacGregor, M. A. 2023, ApJ, 954, 10
Jenkins, J. M., Twicken, J. D., McCauliff, S., et al. 2016, Proc. SPIE, 9913, 99133E
Kallinger, T., Reegen, P., & Weiss, W. W. 2008, A&A, 481, 571
Kawaler, S. D. 2021, RNAAS, 5, 258
Keppler, M., Benisty, M., Müller, A., et al. 2018, A&A, 617, A44
Kouwenhoven, M. B. N., Brown, A. G. A., Zinnecker, H., Kaper, L., & Portegies Zwart, S. F. 2005, A&A, 430, 137
Kraus, S., Le Bouquin, J.-B., Kreplin, A., et al. 2020, ApJL, 897, L8
Kurtz, D. W. 2022, ARA&A, 60, 31
Lagrange, A. M., Bonnefoy, M., Chauvin, G., et al. 2010, Sci, 329, 57
Lagrange, A. M., Gratadour, D., Chauvin, G., et al. 2009, A&A, 493, L21
Lagrange, A. M., Meunier, N., Rubini, P., et al. 2019, NatAs, 3, 1135
Li, G., Van Reeth, T., Bedding, T. R., et al. 2020, MNRAS, 491, 3586
Lightkurve Collaboration, Cardoso, J. V. d. M., Hedges, C., et al. 2018, Lightkurve: Kepler and TESS time series analysis in Python, Astrophysics Source Code Library, ascl:1812.013
Liu, M. C., Dupuy, T. J., & Allers, K. N. 2016, ApJ, 833, 96
Luhman, K. L. 2022, AJ, 163, 24
Macintosh, B., Graham, J. R., Barman, T., et al. 2015, Sci, 350, 64
Mamajek, E. E., Meyer, M. R., & Liebert, J. 2002, AJ, 124, 1670
Marino, S. 2022, arXiv:2202.03053
Marleau, G.-D., Coleman, G. A. L., Leleu, A., & Mordasini, C. 2019, A&A, 624, A20
Marois, C., Macintosh, B., Barman, T., et al. 2008, Sci, 322, 1348
Marois, C., Zuckerman, B., Konopacky, Q. M., Macintosh, B., & Barman, T. 2010, Natur, 468, 1080
Masuda, K., & Winn, J. N. 2020, AJ, 159, 81
McAlister, H. A., ten Brummelaar, T. A., Gies, D. R., et al. 2005, ApJ, 628, 439
McQuillan, A., Mazeh, T., & Aigrain, S. 2014, ApJS, 211, 24
Mesa, D., Gratton, R., Kervella, P., et al. 2023, A&A, 672, A93
Mesa, D., Keppler, M., Cantalloube, F., et al. 2019, A&A, 632, A25
Monnier, J. D., Zhao, M., Pedretti, E., et al. 2007, Sci, 317, 342
Murphy, S. J., Bedding, T. R., Gautam, A., & Joyce, M. 2023, MNRAS, 526, 3779
Murphy, S. J., Bedding, T. R., & Shibahashi, H. 2016, ApJL, 827, L17
Murphy, S. J., Hey, D., Van Reeth, T., & Bedding, T. R. 2019, MNRAS, 485, 2380
Murphy, S. J., Joyce, M., Bedding, T. R., White, T. R., & Kama, M. 2021, MNRAS, 502, 1633
Nagpal, V., Blunt, S., Bowler, B. P., et al. 2023, AJ, 165, 32
Nowak, M., Lacour, S., Lagrange, A. M., et al. 2020, A&A, 642, L2
Ochsenbein, F., Bauer, P., & Marcout, J. 2000, A&AS, 143, 23
O'Neil, K. K., Martinez, G. D., Hees, A., et al. 2019, AJ, 158, 4
Pavlenko, Y., Kulyk, I., Shubina, O., et al. 2022, A&A, 660, A49
Pecaut, M. J., Mamajek, E. E., & Bubar, E. J. 2012, ApJ, 746, 154
Petrus, S., Bonnefoy, M., Chauvin, G., et al. 2021, A&A, 648, A59
Pollack, J. B., Hubickyj, O., Bodenheimer, P., et al. 1996, Icar, 124, 62
Rafikov, R. R. 2011, ApJ, 727, 86
Reegen, P. 2007, A&A, 467, 1353
Reegen, P. 2011, CoAst, 163, 3
Reese, D. R. 2022, FrASS, 9, 934579
Ricker, G. R., Winn, J. N., Vanderspek, R., et al. 2015, JATIS, 1, 014003
Royer, F., Grenier, S., Baylac, M. O., Gómez, A. E., & Zorec, J. 2002, A&A, 393, 897
Sartori, M. J., Lépine, J. R. D., & Dias, W. S. 2003, A&A, 404, 913
Schröder, C., Reiners, A., & Schmitt, J. H. M. M. 2009, A&A, 493, 1099
Sepulveda, A. G., & Bowler, B. P. 2022, AJ, 163, 52
Sepulveda, A. G., Huber, D., Li, G., et al. 2023, RNAAS, 7, 2
Sepulveda, A. G., Huber, D., Zhang, Z., et al. 2022, ApJ, 938, 49
Sikora, J., Wade, G. A., & Rowe, J. 2020, MNRAS, 498, 2456
Smith, J. C., Stumpe, M. C., Van Cleve, J. E., et al. 2012, PASP, 124, 1000
Song, I., Zuckerman, B., & Bessell, M. S. 2012, AJ, 144, 8
Stassun, K. G., Oelkers, R. J., Paegert, M., et al. 2019, AJ, 158, 138
Stassun, K. G., Oelkers, R. J., Pepper, J., et al. 2018, AJ, 156, 102
Steindl, T., Zwintz, K., Müllner, M., et al. 2022, A&A, 664, A32
Stolker, T., Quanz, S. P., Todorov, K. O., et al. 2020, A&A, 635, A182
Stumpe, M. C., Smith, J. C., Catanzarite, J. H., et al. 2014, PASP, 126, 100
Stumpe, M. C., Smith, J. C., Van Cleve, J. E., et al. 2012, PASP, 124, 985
Tetzlaff, N., Neuhäuser, R., & Hohle, M. M. 2011, MNRAS, 410, 190
Uytterhoeven, K., Moya, A., Grigahcène, A., et al. 2011, A&A, 534, A125
van Belle, G. T. 2012, A&ARv, 20, 51
van Belle, G. T., Ciardi, D. R., Thompson, R. R., Akeson, R. L., & Lada, E. A. 2001, ApJ, 559, 1155
Virtanen, P., Gommers, R., Oliphant, T. E., et al. 2020, NatMe, 17, 261
Vousden, W. D., Farr, W. M., & Mandel, I. 2016, MNRAS, 455, 1919
Wang, J. J., Vigan, A., Lacour, S., et al. 2021, AJ, 161, 148
Watson, C. A., Littlefair, S. P., Diamond, C., et al. 2011, MNRAS, 413, L71
Zhang, Z., Mollière, P., Hawkins, K., et al. 2023, AJ, 166, 198
Zieba, S., Zwintz, K., Kenworthy, M. A., & Kennedy, G. M. 2019, A&A, 625, L13
Zwintz, K., Kallinger, T., Guenther, D. B., et al. 2009, A&A, 494, 1031
Zwintz, K., Reese, D. R., Neiner, C., et al. 2019, A&A, 627, A28